

MANTIS: combined x-ray, electron and optical Monte Carlo simulations of indirect radiation imaging systems

This content has been downloaded from IOPscience. Please scroll down to see the full text.

2006 Phys. Med. Biol. 51 1545

(<http://iopscience.iop.org/0031-9155/51/6/013>)

View [the table of contents for this issue](#), or go to the [journal homepage](#) for more

Download details:

IP Address: 146.137.70.71

This content was downloaded on 14/09/2015 at 16:28

Please note that [terms and conditions apply](#).

MANTIS: combined x-ray, electron and optical Monte Carlo simulations of indirect radiation imaging systems

Aldo Badano¹ and Josep Sempau²

¹ NIBIB/CDRH Laboratory for the Assessment of Medical Imaging Systems, 12720 Twinbrook Parkway, HFZ-142, Rockville, MD 20857, USA

² Institut de Tècniques Energètiques, Universitat Politècnica de Catalunya, Diagonal 647, 08028 Barcelona, Spain

E-mail: aldo.badano@fda.hhs.gov and josep.sempau@upc.es

Received 19 September 2005, in final form 25 January 2006

Published 1 March 2006

Online at stacks.iop.org/PMB/51/1545

Abstract

We describe MANTIS (Monte carlo x-ray electron optical Imaging Simulation), a tool for simulating imaging systems that tracks x-rays, electrons and optical photons in arbitrary materials and complex geometries. The x-ray and electron transport and involved physics models are from the PENELOPE package, and the optical transport and corresponding physics models are from DETECT-II and include Fresnel refraction and reflection at material boundaries, bulk absorption and scattering. Complex geometries can be handled with the aid of the geometry routines included in PENELOPE. When x-rays or electrons interact and deposit energy in the scintillator, the code generates a number of optical quanta according to a user-selected model for the conversion process. The optical photons are then tracked until they reach an absorption event, which in some cases contributes to the output signal, or escape from the geometry. We demonstrate the capabilities of this new tool with respect to the statistics of the optical signal detected and to the three-dimensional point-response functions corresponding to columnar phosphor screens.

(Some figures in this article are in colour only in the electronic version)

1. Introduction

Most models of x-ray imaging detectors use limited or no x-ray scatter, no electron transport, and define phosphor blur typically with a Gaussian distribution. Conversion gain in these simple models is taken from a distribution (typically Poisson) and no depth-dependent optical collection efficiencies are used. X-ray scattering in the object and backscattering from non-active detector layers is frequently disregarded. Moreover, these models are usually limited

to normal x-ray incidence. Overall, they cannot accurately represent shift-variant and non-stationary systems.

Although a significant improvement in the treatment of phosphor depth effects, the model presented by our group recently (Gallas *et al* 2004, Badano *et al* 2004) was limited to low x-ray energy where no significant Compton scattering or x-ray fluorescence was present. Electron transport was not considered and phosphor blur was isotropic, obtained with a simplistic columnar model. In addition, no scattering in the object nor in the non-active detector layers was included.

In this paper, we report on an improved simulation tool called MANTIS (Monte carlo x-ray electroN optIcal Imaging Simulation) for modelling imaging systems that includes the transport of x-ray photons, electrons and optical photons within the same geometry. The code MANTIS is the intimate combination of two building blocks: PENELOPE (an x-ray/electron Monte Carlo transport code) and DETECT-II (an optical photon Monte Carlo transport code). It is intended for the study of problems involving indirect imaging sensors in which light is generated by the interaction of particles with matter in a transducer (so-called phosphor or scintillator) material. In MANTIS, the processes of energy transfer from secondary electrons to light is modelled event by event, according to an energy-dependent gain and with a particular model for the variations in the efficiency of that energy transfer. We use MANTIS—from the Greek *prophet* or *oracle*—to investigate imaging characteristics of phosphor screens for digital x-ray imaging systems.

2. The physics models in MANTIS

The validity of MANTIS is limited to ionizing radiation energies above 50 eV and lower than 1 GeV, and to optical photons whose wavelength is small compared to the smallest characteristic dimension of the structures to be modelled. MANTIS includes all the relevant x-ray and electron interactions in the considered energy range. The phosphor blurs obtained with MANTIS are anisotropic and realistic due to improvements in the modelling of the physics, and, in the case of columnar phosphors, by the presence of columnar tilt and a more packed columnar configuration with column-in-centre-and-corners array that closely matches experimentally measured packing fractions.

2.1. X-ray and electron transport

The x-ray and electron transport methods are from the PENELOPE package (Salvat *et al* 2003, Sempau *et al* 1997). The computer code system PENELOPE performs Monte Carlo simulation of coupled electron-photon transport in arbitrarily defined materials in the energy range from 50 eV up to 1 GeV. Photon transport is simulated by means of the detailed simulation scheme, i.e., interaction by interaction. Electron and positron histories are generated on the basis of a mixed procedure, which combines detailed simulation of hard events (those involving energy losses or angular deflections above certain user-defined cut-offs) with condensed simulation of soft interactions. Within the PENELOPE package, the geometry routines (PENGEO) permit the generation of random electron-photon showers in material systems consisting of homogeneous bodies bounded by quadratic surfaces. This package allows for translation and rotation of bodies, which will prove useful for the simulation of many-angle projection imaging systems like computed tomography and tomosynthesis.

In the energy range from 50 eV up to 1 GeV, the dominant interaction processes between photons and matter are coherent (Rayleigh) scattering, incoherent (Compton) scattering, the photoelectric effect and electron-positron pair production. Other interactions occur with much

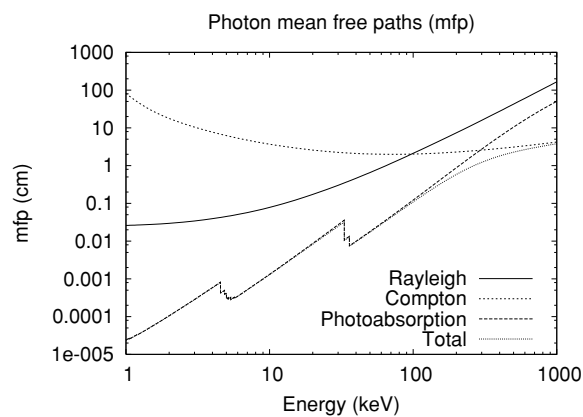


Figure 1. Mean-free path of different photon interaction mechanisms for CsI in the diagnostic imaging energy range, obtained with the program TABLES included in the PENELOPE 2005 package.

smaller probability and can be disregarded in our analysis. From a few keV down to 50 eV the uncertainty in the cross sections is relatively large and, hence, the description of the transport process is semi-quantitative. Even at these low energies, the physics models are among the most reliable available to date and allow us to have a qualitative view of the transport process. For electrons (and positrons) the physics models include elastic scattering, inelastic collisions, bremsstrahlung emission and positron annihilation. The atomic differential cross sections adopted in PENELOPE are defined either as analytical functions or by means of numerical tables, or as a combination of both. The fluorescent radiation (either x-rays or Auger electrons) that results from the relaxation after a vacancy in the K, L, or M atomic shells is also simulated. The detailed description of the physics models are given by (Salvat *et al* 2003) in a document that is published and freely distributed with the PENELOPE code by the Nuclear Energy Agency (NEA). PENELOPE has been applied to a wide range of problems (Siegbahn *et al* 2003, DesRosiers *et al* 2000, Mazurier *et al* 2001, Mourtada *et al* 2003, Al-Dweri and Lallena 2004, Cot *et al* 2004, Moskvina *et al* 2004, Sempau *et al* 2004) and has been validated extensively (Sempau *et al* 2003, Carrasco *et al* 2004, Llovet *et al* 2003).

As an example of the cross sections used in the package, figure 1 shows the mean-free path of x-rays in the diagnostic energy range for the three interaction types: Rayleigh, photoelectric and Compton scattering. The PENELOPE package was adapted to the specific requirements of the MANTIS simulation using PENEASY, a generic main program and accessory routines that allow easy configuration of PENELOPE. PENEASY is freely available from http://www.upc.es/inte/english/download_engALL.htm.

2.2. Optical transport

A detailed description of the optical physics model and the procedures for the definition of periodic geometric structures (such as those found in columnar scintillator screens) are given by (Badano 2003). The optical transport models in MANTIS are taken from DETECT-II, an optical Monte Carlo simulation code for the study of light transport processes within emissive structures (Badano 1999, Badano and Flynn 1997, Badano and Kanicki 1999, 2001). DETECT-II extended previous work on optical Monte Carlo (Knoll and Knoll 1988) by improving the description of optical physics models. Optical processes described in MANTIS include bulk absorption, scattering and Fresnel refraction (Badano 2003). To determine the location

of the next collision (absorption or bulk scattering event), a distance is sampled from an exponential probability density function based on the total mean-free path. If a collision occurs, a decision is made with respect to the type of event based on the relative wavelength-dependent cross sections for absorption and scattering. At optical boundaries, an analysis is performed depending on the surface type and material properties, using Fresnel's equations while considering the polarization of the incoming photon.

The optical transport methods in DETECT-II implemented in MANTIS are based on a set of assumptions. First, we assume validity of the geometrical optics treatment (Born and Wolf 1965) which neglects the effect of finite wavelength. For Monte Carlo simulations, the light ray is assumed to carry one single quanta (light photon). Then, the reflection and transmission coefficients are interpreted as probabilities (Levy-Leblond and Balibar 1990).

Second, materials are considered to be optically isotropic in the sense of having optical properties that are independent of the direction of transport at all energies. This assumption can be considered valid for crystals with uniform cubic lattices (Born and Wolf 1965) such as CsI:Tl. In addition, the emission of light from luminescent centres is considered to be isotropic. Even though certain types of centres are non-isotropic (Nagirnyi *et al* 1994), resulting in preferential polarization directions, it has been shown that light emission from the Tl⁺ centres in CsI:Tl (an example of a non-isotropic centre) is depolarized at $T > 230$ K (Nagirnyi *et al* 1995).

The optical properties of the materials used in the simulation are entered in the input files as spectral tables (i.e., as functions of the optical photon wavelength λ) and include the index of refraction n and the linear absorption coefficient μ_{abs} . The linear scattering coefficient μ_{sca} is entered for a single wavelength and its variation with λ is obtained from the limiting case of Mie theory for small spheres (Rayleigh's law), according to which μ_{sca} is proportional to λ^{-4} (Born and Wolf 1965, Kerker 1969).

Although the angular probability distribution for scattering events has in some cases been assumed to be isotropic (Firbank *et al* 1996), in MANTIS it can be defined by the user as either isotropic or Rayleigh. On average, Rayleigh scattering of unpolarized light has an angular dependence of the type $1 + \cos^2 \theta_s$, where θ_s is the angle between the directions of the incident and scattered photons. For linearly polarized light photons, the probability of scattering is a function of the angle between the polarization vector of the incident photon, and the direction of the scattered photon (χ), according to $\sin^2 \chi$ (Kerker 1969), with an azimuthal deflection angle sampled uniformly in 2π . This expression used in DETECT-II is also incorporated into MANTIS. Although this model is strictly valid only for scattering by free electrons, the agreement between our simulation results and experiments shows that it is also a good approximation for the type of situations we wish to describe, and it is certainly more realistic than using a simple isotropic distribution which is the approach taken by other authors.

Another feature of MANTIS is the available surface models. Surfaces are defined as boundaries between different materials, and can be of the following types: smooth (optically flat), rough, partially absorber/rough reflector, partially absorber/specular reflector, perfect absorber, partially absorber/diffuse reflector, or transparent. In these surface definitions diffuse (also called Lambertian) reflections are based on the probability distribution function

$$p(\phi) = 2 \cos \phi \sin \phi, \quad (1)$$

where ϕ is the angle formed by the reflected photon and the surface normal ($0 < \phi < \pi/2$). In a reference frame with its z axis coincident with the surface normal, ϕ is the polar angle. The corresponding azimuthal reflection angle is sampled uniformly in $(0, 2\pi]$. The Lambertian distribution is independent of the polar angle of the incoming photon. The roughness algorithm is based on the tilting of the surface normal unit vector \mathbf{n} using an isotropically sampled

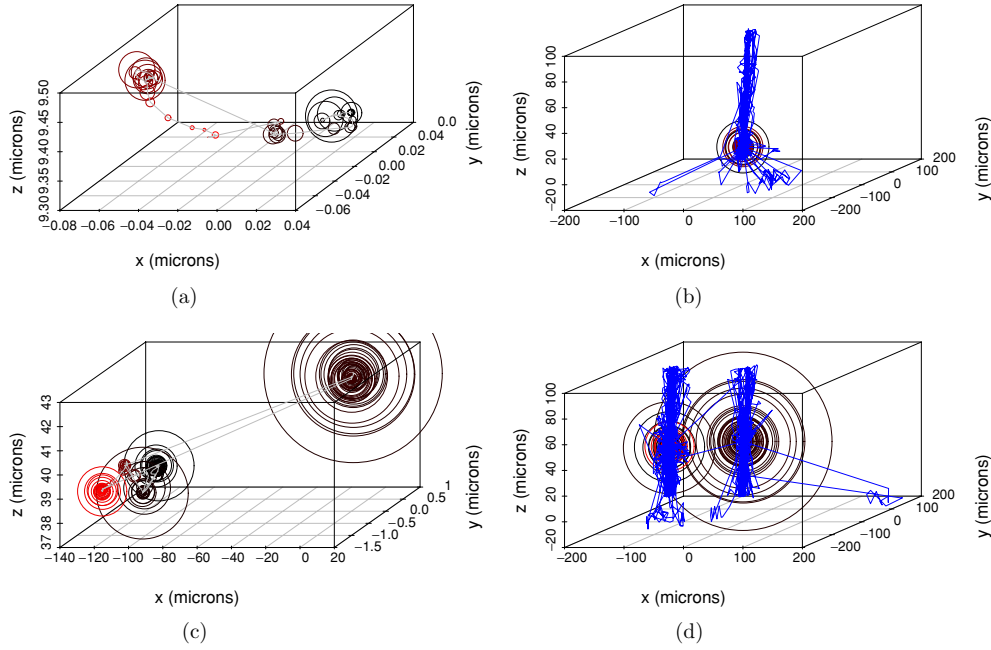


Figure 2. Energy depositions ((a) and (c)) and optical photon trajectories ((b) and (d)) for two sample 39.5 keV x-ray histories in a columnar phosphor. Only the first five optical photon histories are tracked for clarity. The diameter of the circles centred on energy deposition locations are proportional to the deposited energy. Note that in the first example ((a) and (b)), all the energy from the x-ray and secondaries is deposited in one column, while in the second case ((c) and (d)) energy is deposited in two columns. The outline of the columns can be deduced by the multiple reflections of optical photons that occur at their walls.

‘roughness’ unit vector \mathbf{v} , so that the modified (unnormalized) normal direction at the site of boundary crossing of the rough surface is given by $\mathbf{n} + a\mathbf{v}$, where a is a user-adjustable parameter.

The optical characteristics of a surface can be defined in three different ways: (i) by selecting one of the surface models listed above; (ii) assuming a reflective surface with a user-defined reflection coefficient and an explicit angular distribution function for the reflected light rays; or (iii) implicitly, by having recourse to the refraction physics model in MANTIS. This model is based on Fresnel’s formulae for plane waves (Born and Wolf 1965), which provide the independent solutions for the parallel and perpendicular components, relative to the plane of incidence, of the electric field vector of a linearly polarized plane wave associated with a light photon.

The refraction angle θ_2 after a boundary crossing from a material with refractive index n_1 into a material with refractive index n_2 is given by Snell’s law

$$n_1 \sin \theta_1 = n_2 \sin \theta_2, \quad (2)$$

where θ_1 is the incidence angle with respect to the surface normal. According to Fresnel’s formulae, the transmission and reflection probabilities for parallel and perpendicular components are

$$P_{\parallel, \text{trans}} = \frac{\sin(2\theta_1) \sin(2\theta_2)}{\sin^2(\theta_1 + \theta_2) \cos^2(\theta_1 - \theta_2)}, \quad (3a)$$

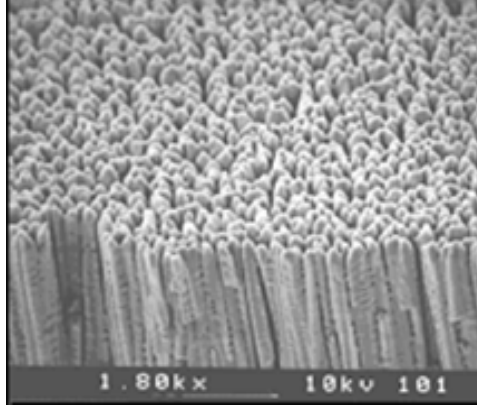


Figure 3. Typical structure of the CsI:Tl needle-like crystals (courtesy of Vivek Nagarkar, RMD Inc.).

$$P_{\perp, \text{trans}} = \frac{\sin(2\theta_1) \sin(2\theta_2)}{\sin^2(\theta_1 + \theta_2)}, \quad (3b)$$

$$P_{\parallel, \text{refl}} = \frac{\tan^2(\theta_1 - \theta_2)}{\tan^2(\theta_1 + \theta_2)} = 1 - P_{\parallel, \text{trans}} \quad (3c)$$

and

$$P_{\perp, \text{refl}} = \frac{\sin^2(\theta_1 - \theta_2)}{\sin^2(\theta_1 + \theta_2)} = 1 - P_{\perp, \text{trans}}. \quad (3d)$$

If ω_{\perp} and ω_{\parallel} are the components of the polarization vector in the perpendicular and parallel directions with respect to a surface ($\omega_{\perp}^2 + \omega_{\parallel}^2 = 1$), we can write the probabilities of reflection and transmission (Born and Wolf 1965) as

$$P_{\text{refl}} = \omega_{\perp}^2 P_{\perp, \text{refl}} + \omega_{\parallel}^2 P_{\parallel, \text{refl}}, \quad (4)$$

with an equivalent expression for the transmitted probability, resulting in

$$P_{\text{trans}} = 1 - P_{\text{refl}}. \quad (5)$$

For the Monte Carlo simulations, we interpret P_{refl} as the probability of reflection, and the fate of the photon is decided with a random number draw. Upon reflection or refraction, the components of the polarization vector are modified. At the first surface encounter, a random linear polarization of the source is assumed to mean that the orientation of a polarization vector normal to the path is random. The polarization of a photon after reflection is given by $\omega'_{\parallel} = \omega_{\parallel} P_{\parallel, \text{refl}}$ and $\omega'_{\perp} = \omega_{\perp} P_{\perp, \text{refl}}$. Similarly, after refraction, $\omega'_{\parallel} = \omega_{\parallel} P_{\parallel, \text{trans}}$ and $\omega'_{\perp} = \omega_{\perp} P_{\perp, \text{trans}}$. The new components are renormalized to yield $\omega_{\parallel}'^2 + \omega_{\perp}'^2 = 1$. For following surface encounters new parallel and perpendicular components are obtained by calculating the polarization vector projected into the surface.

2.3. Coupling between PENELOPE and DETECT-II

In a non-absorbent screen with an ideal sensor (i.e., a screen with an optical collection and optical detection efficiency of 100%), the number of optical photons q generated at each event depositing an energy e is given by

$$q = e\Gamma, \quad (6)$$

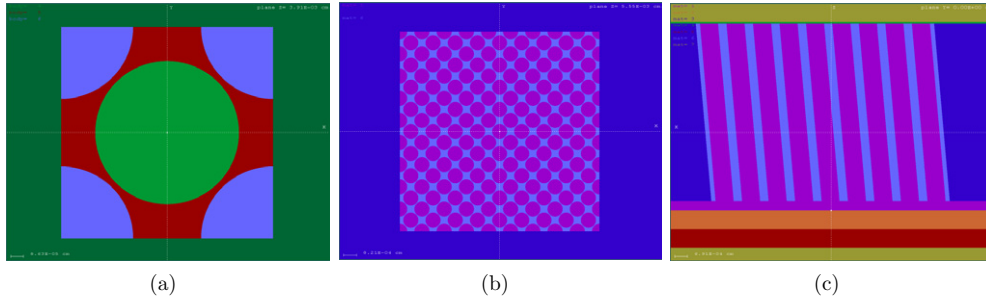


Figure 4. Cross sections of the basic phosphor screen model containing a columnar layer with arbitrary tilt: (a) basic cell for columnar array, (b) top-view of perpendicular column array and (c) array of 5°-tilted columns. Figures obtained with GVIEW (available with PENELOPE's distribution).

where Γ is the optical gain. In MANTIS, Γ is sampled from a user-selected distribution function (which can be a delta, a Poisson, or a Gaussian) with a mean value $\bar{\Gamma}$ given by the material overall gain factor, which is usually assigned from experimental measurements of light output (see, e.g., Knoll 1989). Experimental values of $\bar{\Gamma}$ are reported in the literature (see, for instance, Rowlands and Yorskton 2000). In addition, the user must also provide the spectrum of the light emission in the scintillator. If we assume Poisson gain (Knoll 1989), the optical quanta are Poisson distributed. This approximation is common in simple simulation models. However, due to the optical transport associated with different locations and depths in the phosphor structure, the distribution of detected optical photons does not follow a Poisson form, even at energies where photoelectric effect is predominant.

The optical photons are then tracked (see figure 2) until they reach an absorption event, which in some cases contributes to the output signal, or escape from the geometry. Optical photon trajectories and energy deposition maps for the phosphor model described later in the paper are shown for illustrative purposes in figure 2.

Individual optical photons that reach the photodiode undergo a test for the photo-detection process, by comparing a random number uniformly distributed in (0, 1) to the probability of detection, which corresponds to the spectral sensitivity at the energy of the optical photon (E). If detected, the photon generates a charge (or signal) s given by

$$s = \mathcal{P}(E/\epsilon), \quad (7)$$

where ϵ is the energy required to generate a single electron-hole pair in the photodiode material (for a-Si:H, this value is 3.6 eV) and $\mathcal{P}(x)$ represents the sampling from a Poisson distribution with mean value x . The accumulated signal s is binned in space to obtain the image point-response function, or in pulse-height mode, to obtain the pulse-height spectrum (PHS).

3. Application to columnar phosphors

MANTIS is a simulation tool that can be applied to many imaging problems. Most importantly, the code allows the user to perform deposited energy calculations while, at the same time, obtaining imaging performance metrics. This is of particular relevance to systems that perform radiation therapy treatments with associated imaging capabilities. In the following, we describe how MANTIS can be applied to the modelling of columnar phosphors of the general type used in

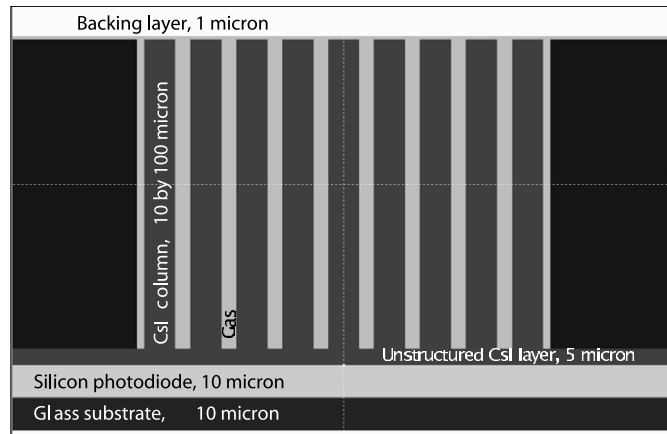


Figure 5. Dimensions and materials in the columnar screen model.

Table 1. Differences between our previous columnar screen model and the model presented in this paper with respect to the validation of computational experiments.

Columnar model in (Badano <i>et al</i> 2004)	Columnar model in this work
Columns with low packing density	Packing density about 85%
Vertical columns	Columns with arbitrary tilt
Columns with flat surfaces	Optically rough surfaces
No electron or fluorescence transport	Complete ionizing radiation transport
Limited to x-ray energies below 30 keV	Wide range of x-ray energies

Table 2. Optical properties of the materials used to define the detector model.

Property	n	$\mu_{\text{abs}} \text{ (cm}^{-1}\text{)}$	$\mu_{\text{sca}} \text{ (cm}^{-1}\text{)}$
Scintillator crystal	1.8	1.0	1.0
Gas	1.0	0.0	0.0
Photodiode	1.7	0.1	10.0

many imaging modalities, including mammography, computed tomography and portal imagers (see figure 3).

Columnar phosphor screens are employed in imaging systems to improve the detection of x-ray quanta while controlling lateral dispersion of the signal due to optical transport (Rowlands and Yorskton 2000, Nagarkar *et al* 1998). Columnar crystalline structures are obtained via a deposition process on specially treated substrates. The modelling of the light transport processes in these types of scintillator structures has been treated before (Badano *et al* 2004) by assuming an unrealistic geometry, among other simplifications (see table 1). With MANTIS, the modelling of such complex structures becomes possible. In the following section, we show results on the imaging performance of these phosphor screens with regard to the statistics of the light output, and to phosphor blur.

We chose to model columnar phosphors for indirect x-ray imaging in front-screen configuration, i.e., with x-rays entering the detector through the phosphor layer and optical quanta being detected by the photo-diode at the opposite side. The screens investigated in

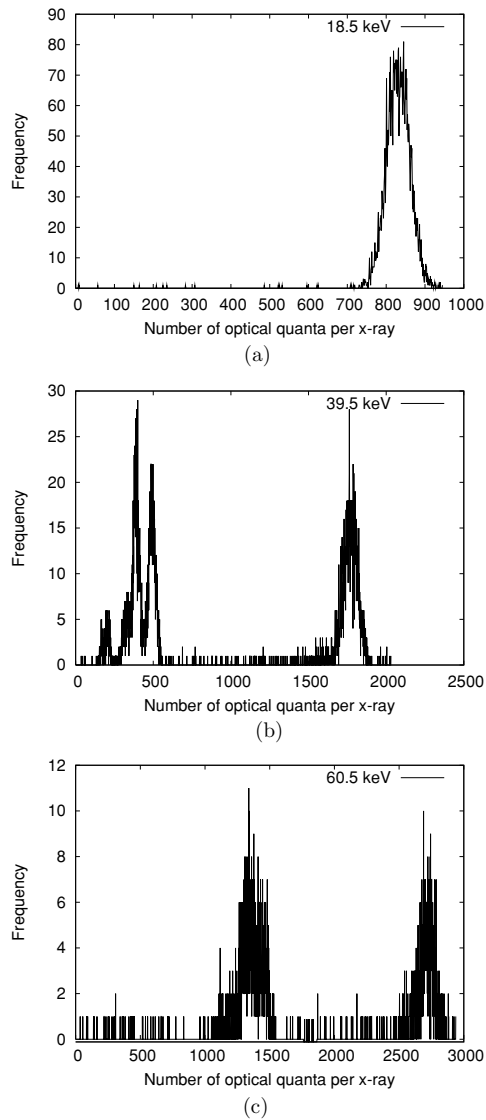


Figure 6. Pulse-height spectra for the columnar model.

this paper have been modelled by a procedure that, instead of trying to replicate experimental measurements on one particular imaging parameter (i.e., modulation transfer function), uses three parameters which, together, represent a more complete description of the imaging characteristics of the phosphor screen. The three performance parameters are the information (Swank) factor I , the light output (either in absolute or relative scales depending on the availability of data from the literature), and the spread function.

In addition, we used information from scanning electron microscopy images of the structure which show that columns are tilted about 5° from the vertical direction, and that a layer of unstructured material is situated at the base of the phosphor in proximity with the

Table 3. Predictions of MANTIS and experimental measurements concerning the statistics of the output signal at different x-ray energies for a 100- μm -thick columnar CsI:Tl phosphor screen model. Experimental Swank factors are from (Zhao *et al* 2004), and optical outputs are from (Zhao 2005). Light output is expressed as a fraction of the generated light quanta, which corresponds to ζ in the treatment of (Gallas *et al* 2004).

X-ray energy	Experimental measurements	MANTIS predictions
18.5 keV		
Information factor	0.9	0.99
Light output (fraction of generated)	0.80	0.77
40.5 keV		
Information factor	0.75	0.73
Light output (fraction of generated)	0.80	0.77
60.5 keV		
Information factor	0.87	0.88
Light output (fraction of generated)	0.80	0.77

sensor material. For clarity, the differences of the model presented here with our previous model for columnar screens (Badano *et al* 2004) are summarized in table 1.

3.1. Columnar geometry

The columnar model, a significant improvement over our previous work (Badano 2003), is based on the generation of geometries using quadratic surfaces and bodies from the Pengeom routines, one of the elements included in the PENELOPE package. The screen is defined by cloning a central cell as many times as necessary (see figure 4). The model dimensions adopted in this paper are shown in figure 5.

Our model of the columnar phosphor, depicted in figure 5, consists of a scintillator crystal, a backing material, a photodiode layer and a glass substrate. The material in between the columns is nitrogen gas. Table 2 lists the optical properties of the materials for each of these layers. Although these properties can be defined as wavelength dependent, we have modelled the detector using a single value of the parameter at 500 nm due to the lack of availability of experimental measurements of wavelength-dependent optical properties for the materials in the form that they are utilized in the screens. The x-ray and electron transport cross sections were obtained using the MATERIAL program included in the PENELOPE package.

The reflection coefficients used in our columnar phosphor model is 1.00 as the reflectivity of the backing surface, and 0.20 for the reflectivity of sensor surface. All surfaces not considered smooth (with implicit refractivity) have a diffuse or Lambertian reflection angular distribution. The optical properties of the top surface of the backing layer and the glass substrate are irrelevant since reflector surfaces are placed at the entrance of these slabs. Therefore, no optical photon travels into those layers.

In all our simulations the coordinate axes are defined as follows: the z axis is perpendicular to interface between the glass and the silicon and, in the section shown in figure 5, points upwards; the x axis points to the left in figure 4, so that the y axis points towards the reader in part (c) of the same figure. Therefore, columns are tilted by turning around the y axis a certain positive (right-hand rule) angle. Any arbitrary tilt can be defined by giving the polar and azimuthal angles of the columns axis direction in the reference frame mentioned above.

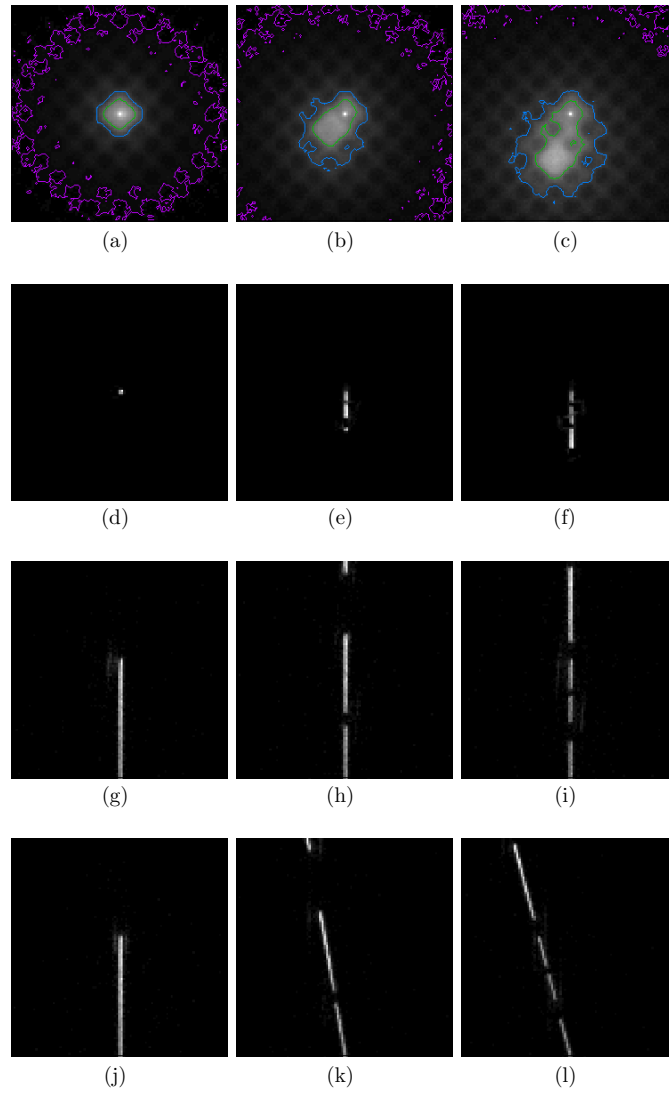


Figure 7. Point-response functions for the columnar phosphor model under normal incidence (first column), 10° (second column) and 15° (third column) x-ray incidence polar angle. In all cases the azimuthal angle of the beam direction was 90° . The first row corresponds to the image in the photodiode layer ($P^{\text{xeo}}(x, y)$), with contour lines indicated for 0.25, 0.1 and 0.01 of the maximum. The second to fourth rows are the projections of P^{xe} into the xy , xz and yz planes, respectively. In the first and second rows the x axis points to the left and the y axis points upwards. In the third row the x axis points to the left and the z axis points upwards. In the fourth row the y axis points to the left and the z axis points upwards.

The results presented in this paper have been obtained with only 1000 x-ray primary histories, which, in turn, spawns about one million optical photon histories. The code was compiled and run in a Linux Beowolf cluster. On average, each x-ray primary (and all its subsequent secondaries) took approximately 2 s to compute, which translates into about 2 ms per optical photon history. Although the statistical uncertainty of the results presented in this paper might not be small enough for final calculation of imaging system

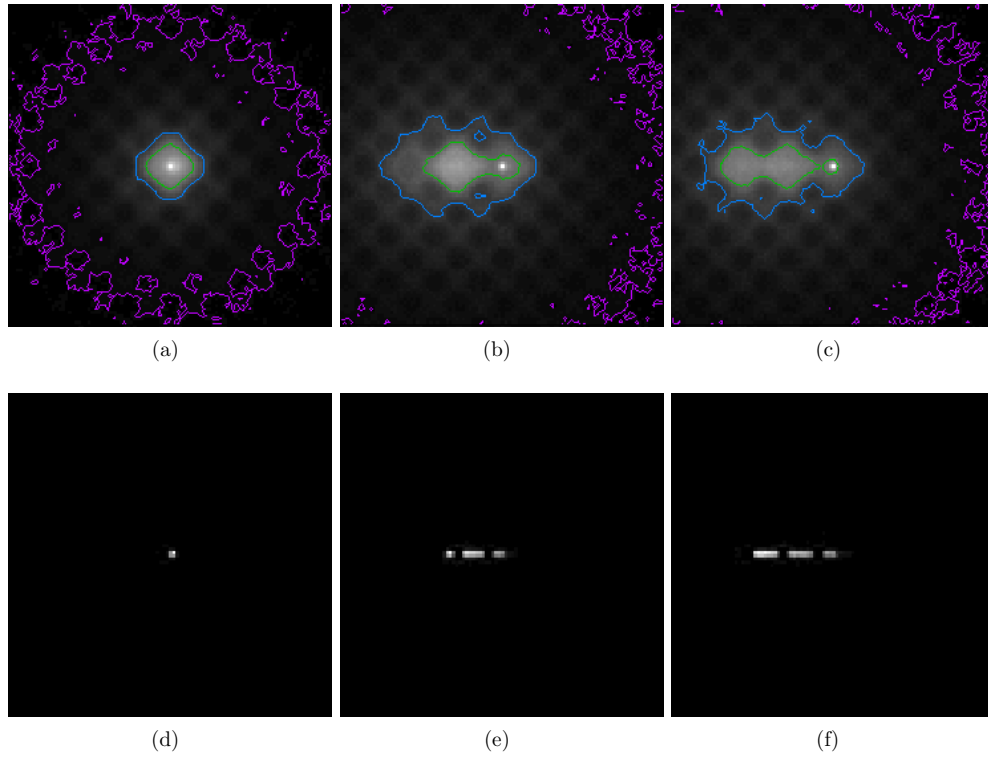


Figure 8. Top view point-response functions for the columnar phosphor model under normal incidence (first column), 10° (second column) and 15° (third column) x-ray incidence polar angle. In all cases the beam azimuthal angle was 180° . The x axis points to the left and the y axis upwards. Contour lines are indicated for 0.25, 0.1 and 0.01 of the maximum. The first row corresponds to the image in the photodiode layer ($P^{\text{xeo}}(x, y)$) and the second row shows the projections of P^{xe} into the xy plane.

performance, they show clear trends and are useful as demonstrations of the capabilities of the code.

3.2. Statistics of the optical signal

With MANTIS, the PHS is obtained directly at the output. From the PHS we can calculate the Swank (Swank 1973) or the information factor I (Ginzburg and Dick 1993) which is given by

$$I = \frac{\langle q \rangle^2}{\langle q^2 \rangle} = \frac{(\int \text{PHS}(q) q \, dq)^2}{\int \text{PHS}(q) \, dq \int \text{PHS}(q) q^2 \, dq}, \quad (8)$$

where q represents the number of detected optical quanta per interaction of primary x-ray.

Figure 6 shows PHSs for mono-energetic beams of different energies. Since the phosphor is mostly transparent, the spectra represent a close indication of the interaction energies. For instance, the four peaks in the left end of the PHS at 39.5 keV correspond to the K- α and K- β transition energies of Cs (30.3 and 34.8 keV) and I (28.0 and 32.1 keV) (National Institute of Standards and Technology 2005). From the distributions in figure 6, and using equation (8), we calculated the information factors and compared them to experimentally measured values reported in the literature (Zhao *et al* 2004). The results are presented in table 3.

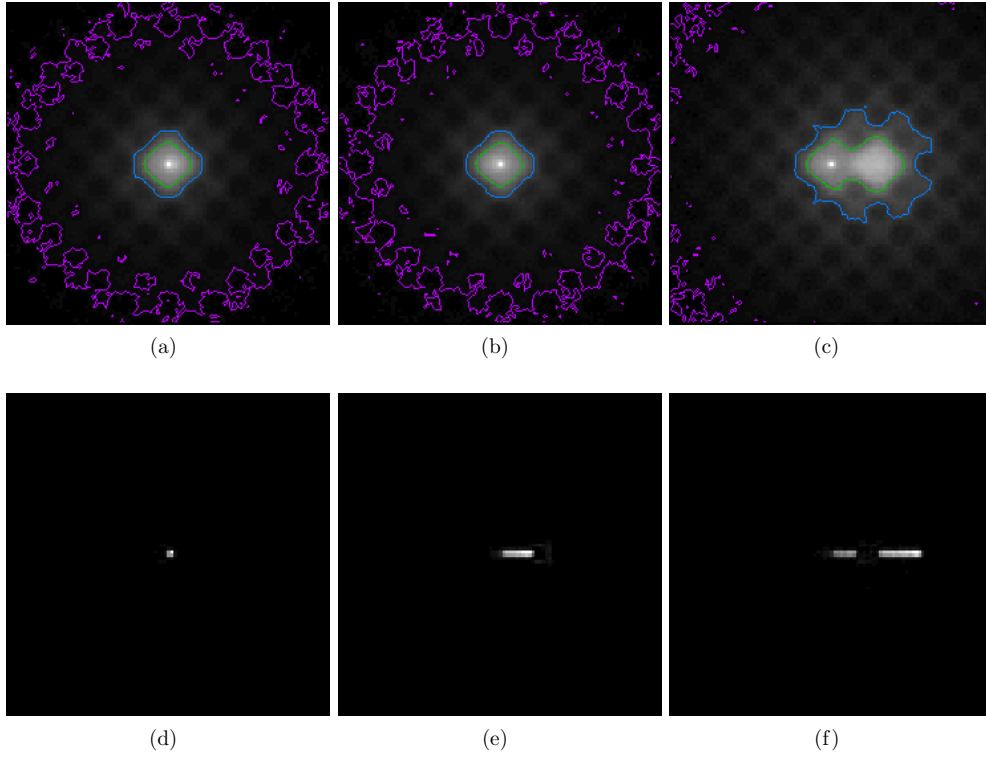


Figure 9. Same details as in figure 8 except that the beam azimuthal angle was 0° .

Note that at 18.5 keV, the experimental measurement system is not capable of capturing such a sharp distribution, which explains the differences between experimental and predicted values of I at this energy (Zhao *et al* 2004).

3.3. Phosphor blur

Another feature of MANTIS is the capability of obtaining the distribution of energy deposited in the phosphor, as well as the image corresponding to the optical signal detected in the photodiode layer. In this section, we present results with respect to the three-dimensional point-response function (3D-PRF). The 3D-PRFs were obtained by counting the energy deposited in a three-dimensional array of cubic bins with a side of $1 \mu\text{m}$.

To illustrate the possibilities of the code, we present results for different angles of incidence of the x-ray photon beam, namely, at normal incidence, 5° , 10° and 15° . Our results are expressed in terms of two components: $P^{\text{xe}}(x, y, z)$, a 3D array of deposited energy associated with x-ray and electron transport, and $P^{\text{xco}}(x, y)$, a two-dimensional array that accumulates the detected optical photons in the photodiode layer (the image). $P^{\text{xco}}(x, y)$ depicts the blur associated with the transport of x-rays, electrons and optical photons. For presentation purposes, we show the projections of the 3D distribution $P^{\text{xe}}(x, y, z)$ into the xz and xy planes. For a phosphor thickness τ , our notation is as follows,

$$P^{\text{xe}}(x, y) = \int_0^\tau P^{\text{xe}}(x, y, z) dz, \quad (9)$$

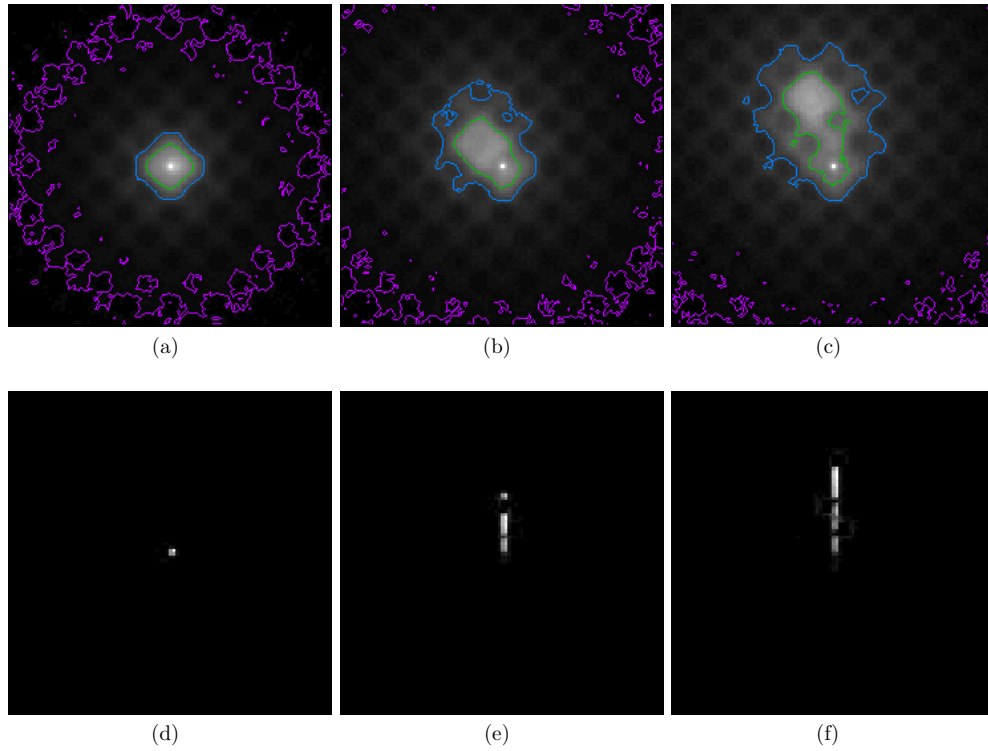


Figure 10. Same details as in figure 8 except that the beam azimuthal angle was 90° .

$$P^{\text{xe}}(y, z) = \int_0^X P^{\text{xe}}(x, y, z) dx, \quad \text{and} \quad (10)$$

$$P^{\text{xe}}(x, z) = \int_0^Y P^{\text{xe}}(x, y, z) dy, \quad (11)$$

with X and Y being the lengths of the screen model along the x and y axes.

Figure 7 shows the distributions for the columnar model for an x-ray energy of 19.5 keV. The first row corresponds to the optical image at the photodiode, $P^{\text{xco}}(x, y)$. In the second, third and fourth row we show $P^{\text{xe}}(x, y)$, $P^{\text{xe}}(x, z)$ and $P^{\text{xe}}(y, z)$, respectively. Due to the column tilt, which was fixed in all our simulations to a polar angle of 5° and an azimuthal angle of 0° with respect to the reference frame defined before, the results are different when the x-ray beam is incident at a certain polar angle but at variable azimuthal angles. To demonstrate this effect figures 8–10 show the top-view projections, similar as those of figure 7, for different orientations of the beam (same polar angle, different azimuthal angles). The ability of the MANTIS package to obtain three-dimensional, depth-dependent point-response functions of deposited energy within the columnar phosphor, while at the same time generating the image recorded in the pixel array, is a major improvement of the code versus previous work from our group and other simulation packages.

Our last result relates to the change in the PRF as the x-ray pencil beam hits different areas of the columns. In figure 11 we observe the variations in PRF as the x-ray beam scans the structure from the centre ($x = 0, y = 0$) to the location ($x = 0, y = 15 \mu\text{m}$) in steps of $3 \mu\text{m}$.

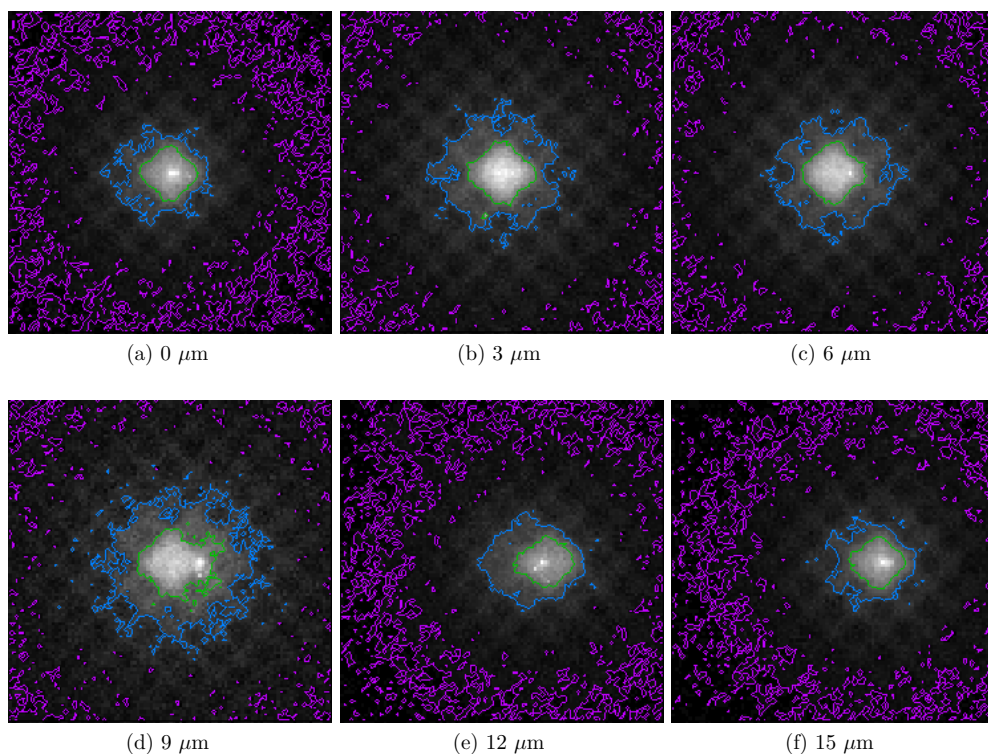


Figure 11. Point-response function $P^{\text{xco}}(x, y)$ as the incidence location of the x-ray beam is scanned over the columnar array toward the right from the centre (a) a distance indicated in each sub-figure caption.

4. Discussion

The simulation tool MANTIS provides new opportunities for the realistic modelling of imaging performance of detectors based on indirect x-ray detection using columnar phosphor screens. For instance, our pulse-height spectra can be used in conjunction with appropriately hardened x-ray spectra to calculate the zero-spatial-frequency detective quantum efficiency of phosphor screens using the approach of Wagner and Tapiovaara (Wagner *et al* 1997) and the methodology reported by our group in 2003 (Jennings and Badano 2003).

Our results suggest, for the first time, that the point-response function is highly non-symmetrical, and that the resolution properties of a columnar screen in a tomographic or tomosynthetic imaging system vary with the angle of x-ray incidence. Predictions from MANTIS, after proper validation, can provide the required understanding of the extent of such variations, and eventually, lead to the incorporation of the angular dependence into the reconstruction algorithms of a volumetric x-ray imaging system. Work to validate the angular dependence of the point-response functions is underway in our laboratories.

The ability of combining, within the same simulation run, features from PENELOPE (i.e., dose scoring in regions of interests) with imaging performance metrics from DETECT-II (i.e., point-response function) allows a more complete treatment of the imaging system for optimization and development of novel x-ray modalities. This ability is no longer limited to low x-ray energies or to normally incident x-ray beams.

Acknowledgments

JS acknowledges partial financial support from the Fondo de Investigación Sanitaria of the Spanish Ministerio de Sanidad y Consumo, project number FIS 03/0980.

References

- Al-Dweri F M and Lallena A M 2004 A simplified model of the source channel of the Leksell gamma knife: testing multisource configurations with PENELOPE *Phys. Med. Biol.* **49** 3441–53
- Badano A 1999 Image quality degradation by light scattering processes in high performance display devices for medical imaging *PhD Thesis* University of Michigan
- Badano A 2003 Optical blur and collection efficiency in columnar phosphors for x-ray imaging *Nucl. Instrum. Methods Phys. Res. A* **508** 467–79
- Badano A and Flynn M J 1997 Monte Carlo modelling of the luminance spread function in flat panel displays *Proc. Int. Display Res. Conf.* **21** 382–5
- Badano A, Flynn M J, Muka E, Compton K and Monsees T 1999 The veiling glare point-spread function of medical imaging monitors *Proc. SPIE* **3658** 458–67
- Badano A, Gagne R M, Gallas B D, Jennings R J, Boswell J S and Myers K J 2004 Lubberts effects in columnar phosphors *Med. Phys.* **31** 3122–31
- Badano A and Kanicki J 1999 Monte Carlo modelling method for light transport in organic thin-film light-emitting devices *Proc. OSA Conf. on Organic Thin Films for Photonics Applications* pp 205–7
- Badano A and Kanicki J 2001 Monte Carlo analysis of the spectral photon emission and extraction efficiency of organic light-emitting devices *J. Appl. Phys.* **90** 1827–30
- Born M and Wolf E 1965 *Principles of Optics* 3rd revised edn (Oxford: Pergamon Press)
- Carrasco P, Jornet N, Duch M A, Weber L, Ginjaume M, Eudaldo T, Jurado D, Ruiz A and Ribas M 2004 Comparison of dose calculation algorithms in phantoms with lung equivalent heterogeneities under conditions of lateral electronic disequilibrium *Med. Phys.* **31** 2899–911
- Cot A, Sempau J, Pareto D, Bullich S, Pavia J, Calviño F and Ros D 2004 Study of the point spread function (PSF) for ^{123}I SPECT imaging using Monte Carlo simulation *Phys. Med. Biol.* **49** 3125–36
- DesRosiers C, Moskvina V, Bielajew A F and Papiez L 2000 150–250 MeV electron beams in radiation therapy *Phys. Med. Biol.* **45** 1781–805
- Firbank M *et al* 1996 An investigation of light transport through scattering bodies with non-scattering regions *Phys. Med. Biol.* **41** 767–83
- Gallas B D, Boswell J S, Badano A, Gagne R M and Myers K J 2004 An energy- and depth-dependent model for x-ray imaging *Med. Phys.* **31** 3132–49
- Ginzburg A and Dick C E 1993 Image information transfer properties of x-ray intensifying screens in the energy range from 17 to 320 keV *Med. Phys.* **20** 1013–21
- Jennings R J and Badano A 2003 Effect on DQE of screen energy weighting in mammography *Proc. SPIE* **5030** 319–26
- Kerker M 1969 *The Scattering of Light* (New York: Academic)
- Knoll G F 1989 *Radiation Detection and Measurements* 2nd edn (New York: Wiley)
- Knoll G F and Knoll T F 1988 Light collection in scintillation detector composites for neutron detection *IEEE Trans. Nucl. Sci.* **35** 872–5
- Levy-Leblond J M and Balibar F 1990 *Quantics* (Amsterdam: North-Holland)
- Llovet X, Sorbier L, Campos C S, Acosta E and Salvat F 2003 Monte Carlo simulation of x-ray spectra generated by kilo-electron-volt electrons *J. Appl. Phys.* **93** 3844–51
- Mazurier J, Gouriou J, Chauvenet B and Barthe J 2001 Calculation of perturbation correction factors for some reference dosimeters in high-energy photon beams with the Monte Carlo code PENELOPE *Phys. Med. Biol.* **46** 1707–17
- Moskvina V, Timmerman R, DesRosiers C, Randall M, DesRosiers P, Dittmer P and Papiez L 2004 Monte Carlo simulation of the Leksell Gamma Knife: II. Effects of heterogeneous versus homogeneous media for stereotactic radiosurgery *Phys. Med. Biol.* **49** 4879–95
- Mourtada F, Soares C G, Seltzer S M, Bergstrom P M Jr, Fernández-Varea J M, Asenjo J and Lott S H 2003 Dosimetry characterization of a ^{32}P source wire used for intravascular brachytherapy with automated stepping *Med. Phys.* **30** 959–71
- Nagarkar V V, Gupta T K, Miller S R, Klugerman Y, Squillante M R and Entine G 1998 Structured CsI(Tl) scintillators for x-ray imaging applications *IEEE Trans. Nucl. Sci.* **45** 492–6

- Nagirnyi V *et al* 1995 Peculiarities of the triplet relaxed excited-state structure and luminescence of a CsI:Tl crystal *J. Phys.: Condens. Matter.* **7** 3637–53
- Nagirnyi *et al* 1994 A new model for the visible emission of the CsI:Tl crystal *Chem. Phys. Lett.* **4-5** 533–8
- National Institute of Standards and Technology 2005 *Physical Reference Data Technical Report*, NIST <http://physics.nist.gov/PhysRefData/>
- Rowlands J A and Yorskton J 2000 *Flat Panel Detectors for Digital Radiography* (Bellingham, WA: SPIE Press) pp 223–328
- Salvat F, Fernández-Varea J M and Sempau J 2003 *PENELOPE, A Code System for Monte Carlo Simulation of Electron and Photon Transport* (Issy-les-Moulineaux, France: OECD Nuclear Energy Agency) (Available in PDF format at <http://www.nea.fr>)
- Sempau J, Acosta E, Baró J, Fernández-Varea J M and Salvat F 1997 An algorithm for Monte Carlo simulation of coupled electron-photon transport *Nucl. Instrum. Methods Phys. Res. B* **132** 377–90
- Sempau J, Andreo P, Aldana J, Mazurier J and Salvat F 2004 Electron beam quality correction factors for plane-parallel ionization chambers: Monte Carlo calculations using the PENELOPE system *Phys. Med. Biol.* **49** 4427–44
- Sempau J, Fernández-Varea J M, Acosta E and Salvat F 2003 Experimental benchmarks of the Monte Carlo code PENELOPE *Nucl. Instrum. Methods Phys. Res. B* **207** 107–23
- Siegbahn E A, Nilsson B, Fernández-Varea J M and Andreo P 2003 Calculations of electron fluence correction factors using the Monte Carlo code PENELOPE *Phys. Med. Biol.* **48** 1263–75
- Swank R K 1973 Calculation of modulation transfer functions of x-ray fluorescent screens *Appl. Opt.* **12** 1865–70
- Wagner B K *et al* 1997 Recent developments in low voltage FED phosphors *Int. Display Res. Conf.* **21** 330–4
- Zhao W 2005 personal communication
- Zhao W, Ristic G and Rowlands J A 2004 X-ray imaging performance of structured cesium iodide scintillators *Med. Phys.* **31** 2594–605